RSC Advances

PAPER

View Article Online
View Journal | View Issue

Cite this: *RSC Adv.*, 2017, **7**, 33012

$CoSb_3$ alloy nanoparticles wrapped with N-doped carbon layers as a highly active bifunctional electrocatalyst for zinc–air batteries

Tian-bo Yang,†[a] Kai-Yuan Zhou,†[b] Guang-Yi Chen,*[b] Wan-Xi Zhang*[ab] and Ji-Cai Liang[ab]

Received 28th April 2017
Accepted 26th June 2017

DOI: 10.1039/c7ra04789d

rsc.li/rsc-advances

Rational design and successful synthesis of highly efficient, long-term stable and low-cost bifunctional electro-catalysts are vital for commercialized application of rechargeable zinc–air batteries. Herein, a series of composite catalysts of different contents of $CoSb_3$ alloy nanoparticles wrapped with N-doped carbon layers ($CoSb_3$@NCL) have been synthesized by a simple one-step pyrolytic process. The optimized catalyst ($CoSb_3$@NCL-30) exhibits excellent catalytic activities for both the ORR and OER in alkaline medium, which can be competitive with the Pt/C catalyst (20%). More importantly, a real rechargeable zinc–air battery with the $CoSb_3$@NCL-30 catalyst serving as an air cathode exhibits outstanding electrochemical properties and excellent cycling stability (the overall increment of the voltage gap was only 0.1 V after 60 hours), making it possible to replace expensive noble metal-based catalysts for actual application in rechargeable zinc–air batteries.

1. Introduction

With the rapid depletion of fossil fuels and increasing concerns about environmental issues, novel rechargeable energy storage and conversion devices with high specific energy, low cost and environmental friendliness have attracted widespread attention.[1] It is notable that metal–air batteries have been regarded as one of the up-and-coming energy storage technologies to meet the demands for portable electronic devices and electric vehicles.[2] Among them, the Zn–air battery has been extensively studied due to its high theoretical energy density, environmental friendliness, low cost, and safety.[3,4] However, the sluggish kinetics of the oxygen reduction reaction (ORR) and oxygen evolution reaction (OER) greatly restrict the application of Zn–air batteries.[5,6] Therefore, rational design and fabrication of novel bifunctional electro-catalysts with high activity, good cycling durability and low cost are vital to effectively improve the performance of rechargeable Zn–air batteries.[7]

So far, the precious metal-based catalysts have been deemed as the most effective electro-catalysts for the ORR and OER.[8–10] However, the scarcity and high cost severely restrict their application to extensive commercialization. Thus, it is a huge demand to synthesize non-precious metal catalysts with the commensurate and even better electro-catalytic activity and durability to Pt or other noble metal catalysts.[11] Recently, some transition metals such as Fe, Co, Ni, and Cu have been used to combine with heteroatom doped carbon materials and shown remarkable oxygen electrocatalytic activity.[12–16] Among these transition metals, cobalt (Co) has an appropriate oxygen electrocatalytic activity and oxygen binding energy.[17] Many reports demonstrated that Co and Co alloys possess excellent bifunctional catalytic activities both for ORR and OER.[18–20] Like cobalt, antimony (Sb) is also a common non-precious metal and widely used in battery and microelectronics industry. For example, lead–antimony (PbSb) alloy and tin–antimony (SnSb) alloy as electrode materials have been used in lead–acid batteries and lithium ion batteries.[21,22] However, there is no report of cobalt–antimony alloys or their composites have been applied in Zn–air batteries.

Herein, a series of composite catalysts of different content of $CoSb_3$ alloy nanoparticles wrapped with N-doped carbon layers have been synthesized *via* a simple one-step pyrolytic process by using cobalt nitrate ($Co(NO_3)_2 \cdot 6H_2O$), potassium antimony oxide tartrate hemihydrates ($C_4H_4KO_7Sb \cdot 0.5H_2O$), β-cyclodextrin (β-CD), and urea ($Co(NH_2)_2$) as solid-phase precursors. The optimized catalyst exhibits bifunctional electrocatalytic activities toward both ORR and OER and excellent performance for rechargeable Zn–air battery. Our work provides a potential substitute to the expensive noble metal-based catalysts and a new synthesis strategy to prepare novel and efficient electrocatalysts for Zn–air battery.

[a]*College of Materials Science and Engineering, Jilin University, Changchun, 130025, China. E-mail: zhangwanxi0626@sina.com*

[b]*School of Automotive Engineering, State Key Laboratory of Structural Analysis for Industrial Equipment, Dalian University of Technology, Dalian, 116024, China. E-mail: chengy@dlut.edu.cn*

† Author contributions: Tian-bo Yang and Kai-Yuan Zhou contributed equally to this work.

2. Experimental section

2.1 Synthesis

All reagents are of analytical grade, obtained from Sinopharm Chemical Reagent Co., Ltd and used without further treatment. The synthetic procedure was described in Scheme 1. Typically, 30 mg of $Co(NO_3)_2 \cdot 6H_2O$ and 103 mg of $C_4H_4KO_7Sb \cdot 0.5H_2O$ were firstly dispersed in 20 mL deionized water with constantly magnetic stirring for 6 h. And then 100 mg of β-CD and 3.0 g of urea were simultaneously added in the above solution. After being sequentially stirred for 12 h, the mixture was thoroughly dried in an oven at 80 °C. The obtained precursor powder was heated from room temperature to 800 °C (5 °C min^{-1}) in N_2 with a flow rate of 50 cm^3 min^{-1} and kept at 800 °C for 60 min in a tube furnace. After natural cooled down to room temperature, the remaining powder was washed with distilled water and alcohol each three times and then dried at 60 °C in vacuum. The resulting sample was named as $CoSb_3$@NCL-30, which "NCL" represents N-doped carbon layers and "30" means 30 mg of $Co(NO_3)_2 \cdot 6H_2O$ was used in the precursor. In order to investigate the influence of different content of $CoSb_3$ nanoparticles on the morphology and electrochemical performance of $CoSb_3$@NCL composite catalysts, other two different amounts of $Co(NO_3)_2 \cdot 6H_2O$ (10 mg and 100 mg, respectively) and corresponding amounts of $C_4H_4KO_7Sb \cdot 0.5H_2O$ (the mole radio of Co to Sb was always fixed in 1 : 3) were also used to prepare composite catalysts. The resulting samples were accordingly named as $CoSb_3$@NCL-10 and $CoSb_3$@NCL-100, respectively. For the sake of comparison, the pristine N-doped carbon layers (NCL) and Co@NCL-30 catalyst obtained without $C_4H_4KO_7Sb \cdot 0.5H_2O$ in the precursor were also prepared *via* the similar process described in Scheme 1. The detail experimental parameters of different samples were given in Table 1.

2.2 Physical characterizations

The X-ray diffraction (XRD) patterns were obtained on a Rigaku/Max-3A with Cu Kα radiation. Scanning electron microscope (SEM) images were acquired on a Supra 55 Sapphire apparatus equipped with energy dispersive X-ray analysis system. Transmission Electron Microscope (TEM) and high-resolution transmission electron microscopy (HRTEM) images were recorded on a JEOL-2010 microscope with an accelerating voltage of 200 kV. X-ray photoelectron spectroscopy (XPS) spectra were collected on multifunctional imaging electron spectrometer (Thermo ESCALAB 250XI). The thermo gravimetric (TG) measurement was performed on a Thermo Gravimetric Analyzer (TA Instruments Q500) from room temperature to 800 °C with a heating rate of 10 °C min^{-1} under air.

2.3 Electrochemical measurements

Linear sweep voltammetry (LSV) was detected on CHI 660E electrochemical station (Shanghai, Chenhua) linked with a rotating disk electrode (RDE) in a typical three-electrode device which glassy carbon (GC) electrode (3 mm in diameter), Pt plate, and Ag/AgCl electrode were employed as the working electrode, counter electrode, and reference electrode, respectively. All of electrodes were immersed in oxygen-saturated 0.1 M KOH solution. The potentials in this work were converted to the reversible hydrogen electrode (RHE) by using the following equation:[23]

$$E_{RHE} = E_{Ag/AgCl} + 0.059pH + 0.197 \quad (1)$$

The working electrode was fabricated as follows: 2.4 mg of prepared catalyst was dispersed in 1 mL of mixture solution (735 μL of water, 205 μL of isopropanol and 60 μL of Nafion (5 wt%, Sigma Aldrich)) by ultrasound (>60 min) to form a homogeneous slurry. Then the electro-catalyst ink (3 μL) was dropped onto the mirror-polished GC electrode and slowly dried at room temperature. The loading of catalyst was 100 μg cm^{-2}. For comparison, the commercial Pt/C catalyst (20 wt%, Johnson Matthey) and IrO_2 (Alfa) were also prepared with the same condition.

For ORR test, the LSV was operated from 1.0 V to 0.3 V (*vs.* RHE) with a scan rate of 10 mV s^{-1} at diverse rotation speed (400, 600, 900, 1200, 1600, 2000 and 2500 rpm). Koutecky–Levich (K–L) plots were evaluated at various potentials (0.30–0.45 V

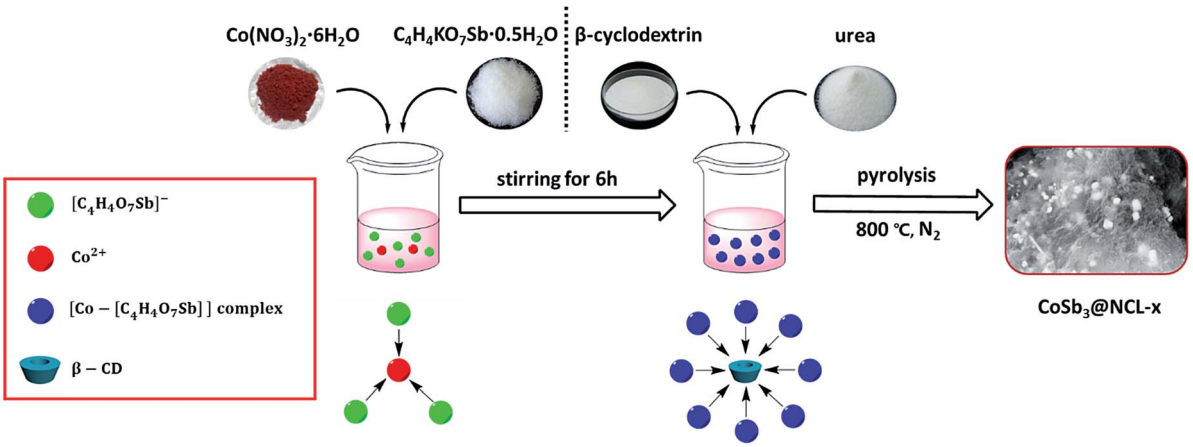

Scheme 1 Synthesis and growth mechanism for the catalysts of $CoSb_3$ alloy nanoparticles wrapped with N-doped carbon layers.

Table 1 Experimental parameters of different catalysts

Sample	$Co(NO_3)_2 \cdot 6H_2O$	$C_4H_4KO_7Sb \cdot 0.5H_2O$	β-CD	Urea
$CoSb_3$@NCL-10	10 mg	34 mg	100 mg	3.0 g
$CoSb_3$@NCL-30	30 mg	103 mg	100 mg	3.0 g
$CoSb_3$@NCL-100	100 mg	343 mg	100 mg	3.0 g
Co@NCL-30	30 mg	0 mg	100 mg	3.0 g
NCL	0 mg	0 mg	100 mg	3.0 g

(*vs.* RHE)). The number of electrons transferred (n) was obtained according to the following K–L formula:

$$j^{-1} = j_L^{-1} + j_K^{-1} = (B\omega^{1/2})^{-1} + j_K^{-1} \quad (2)$$

$$B = 0.2nFC_oD_o^{2/3}\nu^{-1/6} \quad (3)$$

$$j_K = nFkC_o \quad (4)$$

where j, j_K, j_L, and ω are the measured current density, kinetic-limiting current density, diffusion-limiting current density, and the angular velocity, respectively. n, F, C_o, D_o, and ν represent the transferred electron number of the ORR, the Faraday constant, the bulk concentration of O_2, the diffusion coefficient of O_2, and the kinematic viscosity of the electrolyte, respectively. k is the electron-transfer rate constant. For OER analysis, the LSV was measured from 1.0 V to 1.86 V (*vs.* RHE) at 10 mV s^{-1} with the fixed rotating speed of 1600 rpm and O_2-saturated condition.

2.4 Air electrode preparation and zinc–air battery tests

The slurry consists of Vulcan XC-72R and polyvinylidene fluoride (PVDF) with a mass ratio of 8 : 1 was coated onto the carbon paper (Toray TGP-H-060) to form the air diffusion layer. The loading of slurry was about 2 mg cm^{-2}. The catalyst ink was prepared by ultrasonic dispersion of 20 mg $CoSb_3$@NCL-30 catalyst in the mixture of isopropanol (900 μL) and 5 wt% Nafion solution (100 μL). The 200 μL of the above catalyst ink was painted on the air diffusion layer and dried in vacuum at room temperature. The loading of the catalysts were about 1 mg cm^{-2}. For comparison, the commercial Pt/C catalyst-based air electrode was also fabricated under the same manner.

The tests of rechargeable Zn–air battery were executed on a homemade device. The zinc plate, air electrode, and 6 M KOH with 0.2 M zinc acetate solution were served as the anode, the cathode, and electrolyte, respectively. Polarization and long-time galvanostatic charge–discharge tests were executed by CHI 660E electrochemical station with continuous oxygen supply from ambient air.

3. Results and discussion

3.1 Formation mechanism and structural characterization

The possible formation mechanism of the $CoSb_3$@NCL samples could be described by Scheme 1. Firstly, Co^{2+} and $[C_4H_4O_7Sb]^-$ derived from antimony potassium attracted each other by electrostatic field to form the Co–$[C_4H_4O_7Sb]$ complex in water solution. Then, β-CD (C source) and urea (N source) were added to the above solution. The β-CD molecules would successively coordinate with Co–$[C_4H_4O_7Sb]$ by the hydroxyls to further form [(β-CD)–Co–$[C_4H_4O_7Sb]$] complex.[24,25] Finally, after being thoroughly dried, the obtained precursor was pyrolyzed at 800 °C for 1 h in N_2 atmosphere. During this step, the N-doped carbon layers (NCL) derived from β-CD and urea can simultaneously reduce Co–$[C_4H_4O_7Sb]$ complex to $CoSb_3$ alloy, resulting in the formation of $CoSb_3$@NCL nanocomposites.[26] The possible reaction process can be described as follows:

$$[C_4H_4O_7Sb]^- + Co^{2+} \downarrow$$

$$[Co{-}[C_4H_4O_7Sb]]\ \text{complex}\ \ \beta\text{-CD} + \downarrow \quad (5)$$

$$[(\beta\text{-CD}){-}Co{-}[C_4H_4O_7Sb]]\ \text{complex}\ \ H_2NCONH_2 + \downarrow \quad (6)$$

$$CoSb_3@NCL \quad (7)$$

The crystal phase structure of the different catalysts prepared at 800 °C for 1 h in N_2 was firstly identified by XRD. As presented in Fig. 1, all diffraction peaks of $CoSb_3$@NCL-30 can be readily indexed to the cubic phase of $CoSb_3$ alloy (JCPDS no. 88-2437). No other characteristic peaks belong to Co, Sb, and their oxides are observed, indicating that the precursor has been completely reduced to $CoSb_3$ alloy and then well protected by the carbon layers and inert N_2 atmosphere. For comparison, the Co@NCL-30 and NCL samples were also characterized by XRD. The

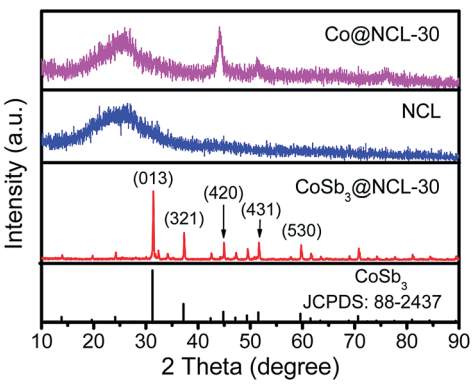

Fig. 1 XRD patterns of $CoSb_3$@NCL-30, Co@NCL-30, and NCL.

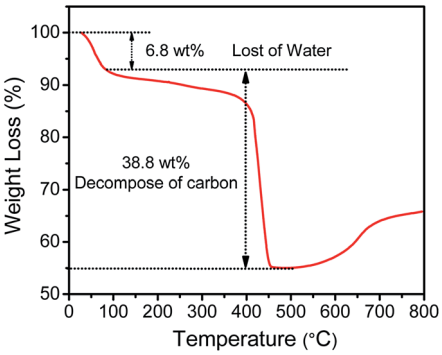

Fig. 2 TG curve of $CoSb_3$@NCL-30 with a heating rate of 10 °C min^{-1} under air.

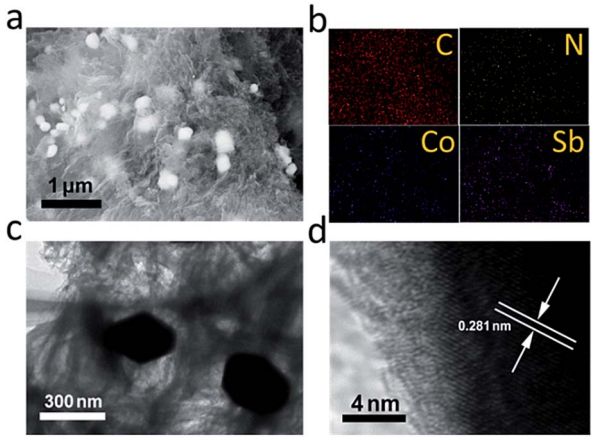

Fig. 4 (a) SEM image; (b) elemental mapping images; (c) TEM image; (d) HRTEM image of $CoSb_3$@NCL-30.

diffraction peaks of Co@NCL-30 can be indexed to the metallic cobalt (JCPDS no. 15-0806) and the broad diffraction peak at ~26° appeared simultaneously in the XRD patterns of Co@NCL-30 and NCL samples could be ascribed to the (002) plane of carbon materials. The $CoSb_3$ content of the $CoSb_3$@NCL-30 composite was determined by thermogravimetric analysis (Fig. 2). According to TG result, the content of $CoSb_3$ is calculated to be about 58.3 wt%. Need to be explained, the last weight increase in TG curve can be attributed to the high temperature oxidation of alloy nanoparticles under air condition.

The XPS was carried out to identify the chemical composition and the bonding configuration of the $CoSb_3$@NCL-30. In the survey spectra (Fig. 3a), the results reveal the existence of C (284.8 eV), N (398.8 eV), Sb (531.3 eV) and Co (780.7 eV) elements, which are in line with the results of XRD. In the high-resolution C 1s spectra (Fig. 3b), a set of peaks at 284.6, 285.4, 286.5, 289.3 and 292.7 eV belong to C=C, C–C, C–N, O=C–O, and π–π*, respectively, implying that the N element is successfully doped in carbon layers.[27,28] Specifically, the π–π* peak (at 292.7 eV) demonstrates that the carbon layers is formed with graphitic-like structure.[28] The high-resolution N 1s spectra (Fig. 3c) can be fitted to four N types: pyridinic N (398.2 eV), pyrrolic N (399.3 eV), graphic N (400.6 eV) and oxidized N (404.6 eV).[29,30] It has been reported that the graphic N could greatly increase the limiting current density and the pyridinic N could improve the onset potential.[30] In the high-resolution Co 2p spectra (Fig. 3d), the peaks with the binding energies of 780.4 and 778.6 eV are attributed to the Co $2p_{3/2}$ of Co(II) and Co(0), respectively. Moreover, the peaks at 782.6 and 785.2 eV should be the satellite peaks of Co $2p_{3/2}$ peaks.[28]

Detailed morphological and structure data of the $CoSb_3$@NCL-30 were characterized by SEM and TEM. SEM images (Fig. 4a) indicates that $CoSb_3$ alloy nanoparticles with the diameter of 200–300 nm are well dispersed in the carbon matrix to form nanocomposites. The corresponding elemental mapping images also confirm the homogeneous distribution of Co, Sb, and N elements in carbon matrix (Fig. 4b). According to the EDS results, the N contents of $CoSb_3$@NCL-10, $CoSb_3$@NCL-30, and $CoSb_3$@NCL-100 are 5.64%, 5.26% and 3.12%, respectively. The results demonstrate that although under the same experimental conditions of temperature, time and the same amount of β-CD and urea in the precursor, the N contents present a gradually downward trend with the increase of the amount of metal salts in the precursor. Because of the metal salts can be completely converted into alloy nanoparticles in the final product by the pyrolytic process, so it also means that the N content is decreased with the increase of the amount of $CoSb_3$ nanoparticles in the composites, which is similar to some previous reports.[31] The TEM image (Fig. 4c) show that the $CoSb_3$

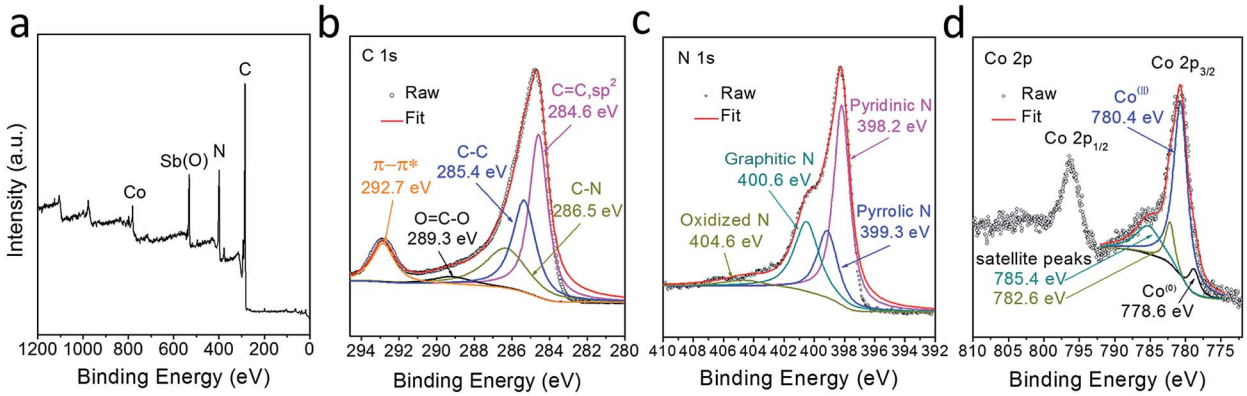

Fig. 3 XPS spectrum of $CoSb_3$@NCL-30. (a) Survey spectra and high-resolution spectra of (b) C 1s, (c) N 1s, (d) Co 2p.

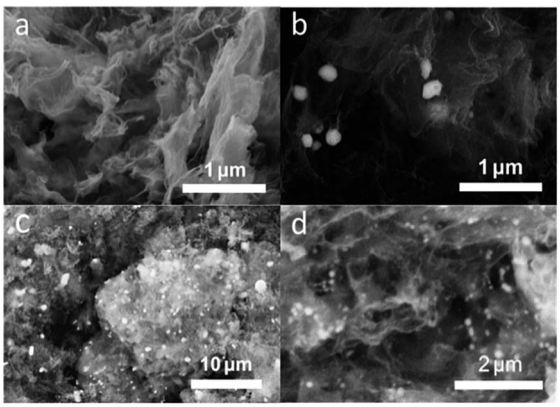

Fig. 5 SEM images of (a) NCL; (b) $CoSb_3$@NCL-10; (c) $CoSb_3$@NCL-100; (d) Co@NCL-30.

alloy nanoparticles are encapsulated in flexible carbon nanolayers and HRTEM image (Fig. 4d) unambiguously reveals the lattice fringe with *d*-spacing of 0.281 nm correspond to the (013) plane of $CoSb_3$. The unique structure $CoSb_3$ alloy nanoparticles wrapped with N-doped carbon nanolayers can not only enable faster transfer of electrons but also avoid agglomeration of alloy nanoparticles during the electrocatalytic reaction and charge–discharge process.[32] For comparison, the morphology of other catalysts (including $CoSb_3$@NCL-10, $CoSb_3$@NCL-100, Co@NCL-30, and NCL) were also characterized and shown in Fig. 5. Among of them, NCL, which was prepared without any metal salts in the precursor, presents a graphene-like structure (Fig. 5a). When different amounts of $Co(NO_3)_2 \cdot 6H_2O$ and $C_4H_4KO_7Sb \cdot 0.5H_2O$ were introduced to the reaction system, the composite catalysts consist of $CoSb_3$ (or Co) nanoparticles and carbon layers can be obtained. The quantity of the $CoSb_3$ nanoparticles in the composite catalysts and the morphology of carbon are relevant to the amounts of $Co(NO_3)_2 \cdot 6H_2O$ and $C_4H_4KO_7Sb \cdot 0.5H_2O$ in the precursor. The $CoSb_3$@NCL-10 shows a similar morphology to that of $CoSb_3$@NCL-30 except for the different quantity of nanoparticles in the composites (Fig. 5b). However, the $CoSb_3$@NCL-100 sample presents a quite different morphology compared to other $CoSb_3$@NCL samples, in which the size of alloy nanoparticles became very large and the carbon morphology also changed from graphene-like nanolayers to irregular bulks (Fig. 5c).

3.2 Electrochemical studies

The bifunctional catalytic capabilities of the oxygen electrocatalysts toward both ORR and OER are very important to rechargeable Zn–air batteries. LSV connected with a RDE was used to evaluate the electrocatalytic performance of different prepared catalysts and the benchmark Pt/C (20%) and IrO_2 catalysts. Polarization curves for ORR in 0.1 M KOH electrolyte (O_2-saturation) at the rotating speed of 1600 rpm are given in Fig. 6a. Among of all the prepared catalysts, the $CoSb_3$@NCL-30

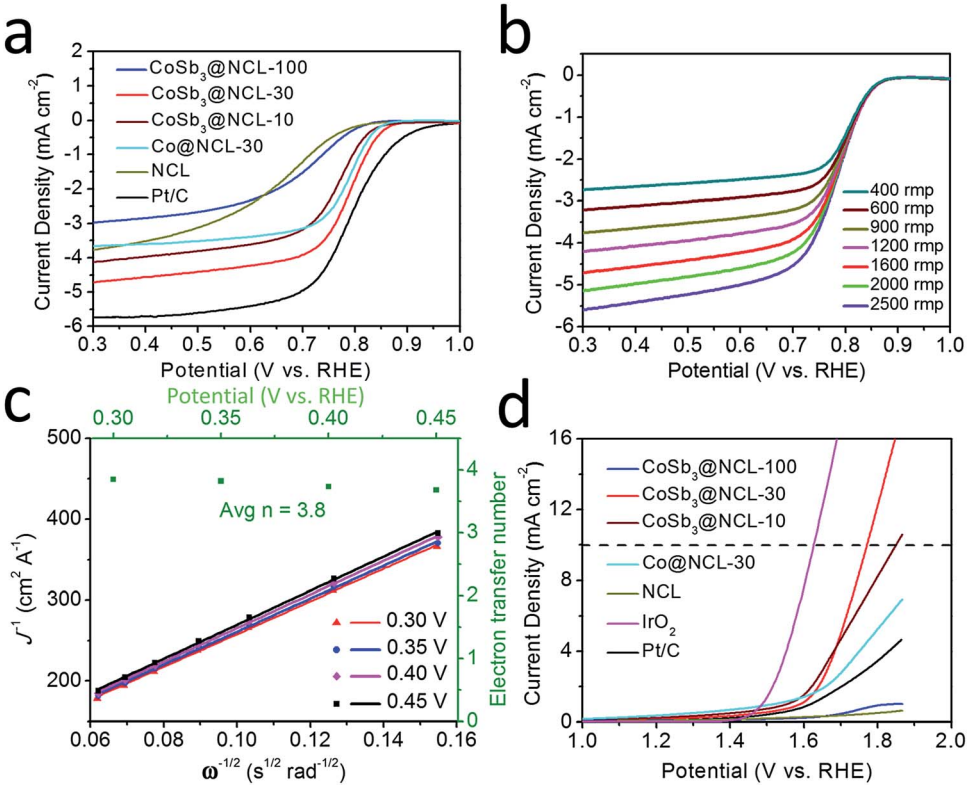

Fig. 6 Electrochemical characterizations of different catalysts. (a) ORR polarization curves of different catalysts at 1600 rpm. (b) ORR polarization curves of $CoSb_3$@NCL-30 at different rotating rates. (c) The corresponding K–L plots of $CoSb_3$@NCL-30 at different potentials (the green dots is the electron transfer number (*n*) per oxygen molecule (O_2) at different potentials). (d) LSV curves of different catalysts for OER at 1600 rpm.

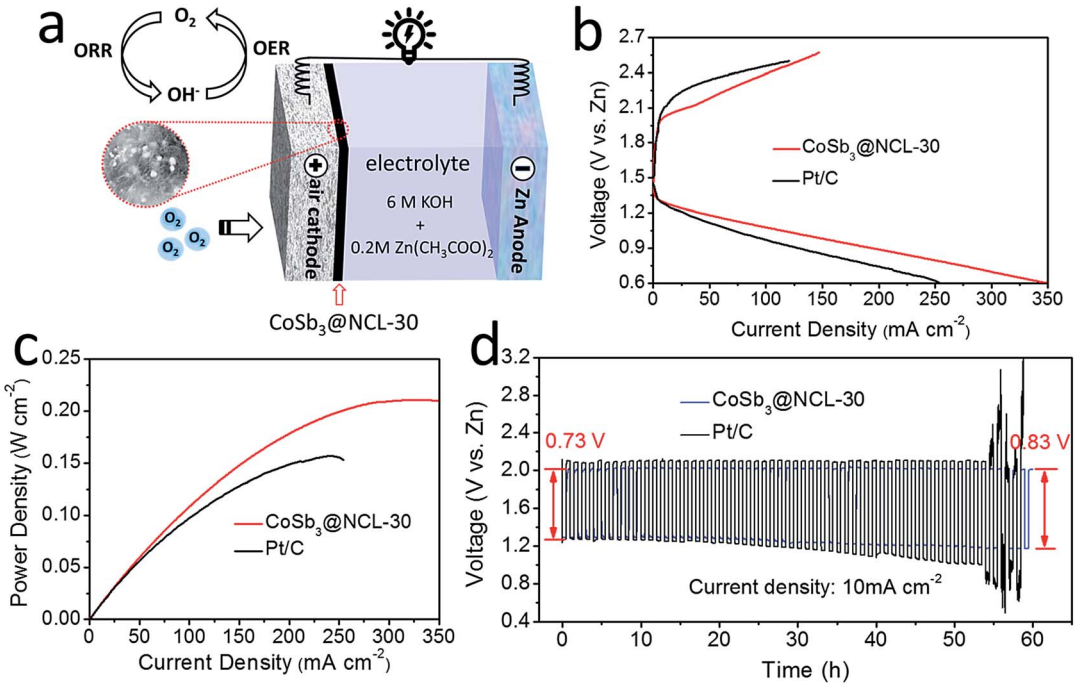

Fig. 7 Zn–air batteries performances. (a) Schematic representation of rechargeable Zn–air battery. (b) Discharge and charge polarization plots of the Zn–air batteries based on $CoSb_3$@NCL-30 catalyst and Pt/C. (c) Corresponding power density plots of the Zn–air batteries based on $CoSb_3$@NCL-30 catalyst and Pt/C. (d) Cycling performance of rechargeable Zn–air batteries based on $CoSb_3$@NCL-30 catalyst and Pt/C at 10 mA cm^{-2} (30 min discharge followed by 30 min charge in each cycle).

exhibits a remarkable ORR activity, only has a slightly lower half-wave potential (0.78 V) and small decrease of limiting diffusion current density (4.71 mA cm^{-2}) compared to commercial Pt/C (0.79 V and 5.74 mA cm^{-2}, respectively) at the same condition. In order to further study the ORR kinetics of $CoSb_3$@NCL-30, RDE tests were carried out at various rotating speed from 400 rmp to 2500 rmp (Fig. 6b). The corresponding K–L plots are provided in Fig. 6c. The linearity and near parallelism of K–L plots indicate a first-order reaction kinetics to the concentration of O_2 dissolved in the electrolyte. The number of electrons transferred (n) is calculated to be about 3.8 at the potentials range from 0.30 to 0.45 V (*vs.* RHE) by using the above K–L formula. This approximately 4-electron transfer pathway of $CoSb_3$@NCL-30 is very critical for Zn–air battery application. Just like ORR determines the discharge performance, OER, which governs the charge performance, is also very important to rechargeable Zn–air battery. The OER catalytic activity of prepared $CoSb_3$@NCL catalysts, Pt/C, and IrO_2 were also

Table 2 A comparison of the Zn–air battery performance of this work with recent relevant literatures

Catalysts	Loading[a] (μg cm^{-2})	Half-wave potential (V *vs.* RHE)	Cycling current (mA cm^{-2})	Cycle time (h)	Fluctuation of discharge potential (E_{DP})/V (initial/end)	Fluctuation of charge potential (E_{CP})/V (initial/end)	Fluctuation of voltage gap V ($\Delta E_{CP} - \Delta E_{DP}$)	Source
Ni/NiO/$NiCo_2O_4$/N-CNT-As	240/300	0.74	5 (A g^{-1})	70	1.20/1.14	1.95/1.94	0.05	Ref. 36
LTFO-C[b]	—/1180	0.72	5 (A g^{-1})	6	~1.24/1.20	~1.88/1.90	0.06	Ref. 37
NCNT/CoO–NiO–NiCo	210/530	0.83	20	17	~1.11/1.06	~2.03/1.97	Negligible change	Ref. 38
Fe@N–C	249/2200	0.83	10	16.7	1.25/1.11	1.95/1.97	0.16 V	Ref. 39
Co–PDA–C	500/1000	0.77	2	500	1.21/1.01	2.15/2.18	0.23 V	Ref. 40
$CoMn_2O_4$/N-rGO	—/1180	—	20	~16.7	~1.09/1.01	~1.77/1.89	0.20 V	Ref. 41
CoS_2(400)/N,S-GO	536/1710	0.79	10	3.3	~1.16/1.10	~1.93/1.88	Negligible change	Ref. 42
FeCo@NC-750	800/1000	0.80	10	20	~1.21/1.14	~1.96/2.00	0.11 V	Ref. 19
$NiCo_2O_4$–CNTs	100/2000	0.80	10	40	~1.30/1.22	~2.08/2.17	0.17 V	Ref. 43
$CoSb_3$@NCL-30	100/1000	0.79	10	60	1.29/1.18	2.02/2.01	0.10 V	This work

[a] The front loading data is used in RDE tests and the rear loading data is used is Zn–air batteries. [b] LTFO-C is the abbreviation of $LaTi_{0.65}Fe_{0.35}O_{3-\delta}$ nanoparticle-decorated nitrogen-doped carbon nanorods.

studied and the corresponding LSV curves are given in Fig. 6d. Obviously, the $CoSb_3$@NCL-30 also shows the best OER performance among all the prepared catalysts, which is just slightly worse than IrO_2 and comparable to the catalysts reported by previous works.[28,33–35] Thanks to the good ORR and OER catalytic activities, the obtained bifunctional $CoSb_3$@NCL-30 catalyst and the commercial Pt/C as the contrast were further used as air cathodes to construct homemade two-electrode rechargeable Zn–air batteries, respectively (Fig. 7a). The corresponding discharge and charge polarization curves of $CoSb_3$@NCL-30 and Pt/C are presented in Fig. 7b. From it, we can clearly find that the $CoSb_3$@NCL-30 cathode shows a better discharge and charge curve compared to commercial Pt/C, with a smaller charge–discharge voltage gap and better round-trip efficiency. Furthermore, the maximum peak power density of $CoSb_3$@NCL-30 (211 mW cm^{-2}) is also higher than that of Pt/C (152 mW cm^{-2}) (Fig. 7c). Long-term stability is also a key factor for the actual application of rechargeable Zn–air battery. The cycling durability of $CoSb_3$@NCL-30 and the benchmark Pt/C were assessed by galvanostatic discharge–charge cycling tests (30 min discharge followed by 30 min charge in each cycle) operated at the current density of 10 mA cm^{-2} (Fig. 7d). It is clearly seen that the $CoSb_3$@NCL-30 catalyst has a better cycling performance compared to Pt/C under the same condition. The initial discharge and charge potential of $CoSb_3$@NCL-30 are 1.29 V and 2.02 V, respectively, indicating a voltage gap of 0.73 V and a round-trip efficiency of 64%. After 60 hours, only slight performance degradation was detected on $CoSb_3$@NCL-30 cathode (the overall increment in the voltage gap was only 0.1 V). The excellent performance of Zn–air battery based on $CoSb_3$@NCL-30 catalyst is comparable or even better than many reported relevant works (Table 2). Due to its high bifunctional ORR/OER electrocatalytic activity, excellent cycling stability, and low-cost, the $CoSb_3$@NCL-30 catalyst has more practical application value in Zn–air battery than those noble metal-based catalysts.

4. Conclusion

In summary, a novel and efficient catalyst of $CoSb_3$ alloy nanoparticles wrapped with N-doped carbon layers was successfully synthesized by a convenient one-step pyrolytic process of solid-phase precursor. The optimized $CoSb_3$@NCL-30 catalyst exhibits excellent high bifunctional electrocatalytic activities both to ORR and OER in alkaline medium. The excellent electrocatalytic performance of $CoSb_3$@NCL-30 can be attributed to the synergistic effect of the hybrid nanostructure. The outer N-doped carbon layers can not only facilitate electron transfer but also reduce the aggregation of $CoSb_3$ nanoparticles to significantly increase the density of active sites. The outstanding electrochemical properties of $CoSb_3$@NCL-30 were further proved in a rechargeable Zn–air battery by a discharge–charge cycling test operated at the current density of 10 mA cm^{-2} for 60 hours under ambient air. Considering the low-cost and simple synthetic method, our work provides a new strategy to large-scale synthesis of advanced bifunctional electrocatalysts to replace the noble metal-based catalysts for rechargeable Zn–air batteries.

Acknowledgements

The authors are grateful to the Fundamental Research Funds for the Central Universities (No. DUT17LK01).

References

1 M. Winter and R. J. Brodd, *Chem. Rev.*, 2004, **104**, 4245–4269.
2 M. A. Rahman, X. Wang and C. Wen, *J. Electrochem. Soc.*, 2013, **10**, A1759–A1771.
3 Y. Li and H. Dai, *Chem. Soc. Rev.*, 2014, **43**, 5257–5275.
4 J. Fu, Z. P. Cano, M. G. Park, A. Yu, M. Fowler and Z. Chen, *Adv. Mater.*, 2016, **29**, 1604685.
5 C. Zhu, H. Li, S. Fu, D. Du and Y. Lin, *Chem. Soc. Rev.*, 2016, **45**, 517–531.
6 S. Zhang, Y. Shao, G. Yin and Y. Lin, *J. Mater. Chem. A*, 2013, **1**, 4631.
7 Y. Li, M. Gong, Y. Liang, J. Feng, J. E. Kim, H. Wang, G. Hong, B. Zhang and H. Dai, *Nat. Commun.*, 2013, **4**, 1805.
8 T. Yu, D. Y. Kim, H. Zhang and Y. Xia, *Angew. Chem., Int. Ed. Engl.*, 2011, **50**, 2773–2777.
9 C. W. Xu, H. Wang, P. K. Shen and S. P. Jiang, *Adv. Mater.*, 2007, **19**, 4256–4259.
10 Y. Lee, J. Suntivich, K. J. May, E. E. Perry and Y. Shao-Horn, *J. Phys. Chem. Lett.*, 2012, **3**, 399–404.
11 R. Cao, J.-S. Lee, M. Liu and J. Cho, *Adv. Energy Mater.*, 2012, **2**, 816–829.
12 P. Ganesan, P. Ramakrishnan, M. Prabu and S. Shanmugam, *Electrochim. Acta*, 2015, **183**, 63–69.
13 J. Deng, L. Yu, D. Deng, X. Chen, F. Yang and X. Bao, *J. Mater. Chem. A*, 2013, **1**, 14868.
14 L. Feng, Y. Liu and J. Zhao, *Phys. Chem. Chem. Phys.*, 2015, **17**, 30687–30694.
15 J. Cho and J.-s. Lee, *ACS Nano*, 2015, **9**, 6493–6501.
16 M. Wu, Q. Tang, F. Dong, Y. Wang, D. Li, Q. Guo, Y. Liu and J. Qiao, *Phys. Chem. Chem. Phys.*, 2016, **18**, 18665–18669.
17 J. K. Nørskov, J. Rossmeisl, A. Logadottir and L. Lindqvist, *J. Phys. Chem. B*, 2004, **108**, 17886–17892.
18 G. Zhang, W. Lu, F. Cao, Z. Xiao and X. Zheng, *J. Power Sources*, 2016, **302**, 114–125.
19 P. Cai, S. Ci, E. Zhang, P. Shao, C. Cao and Z. Wen, *Electrochim. Acta*, 2016, **220**, 354–362.
20 Y. Hou, H. Yuan, Z. Wen, S. Cui, X. Guo, Z. He and J. Chen, *J. Power Sources*, 2016, **307**, 561–568.
21 Y. Chang, X. Mao, Y. Zhao, S. Feng, H. Chen and D. Finlow, *J. Power Sources*, 2009, **191**, 176–183.
22 H. Li, Q. Wang, L. Shi, L. Chen and X. Huang, *Chem. Mater.*, 2002, **14**, 103–108.
23 M. Shen, C. Ruan, Y. Chen, C. Jiang, K. Ai and L. Lu, *ACS Appl. Mater. Interfaces*, 2015, **7**, 1207–1218.
24 G.-Y. Chen, B. Deng, G.-B. Cai, W.-F. Dong, W.-X. Zhang and A.-W. Xu, *Cryst. Growth Des.*, 2008, **8**, 2137–2143.
25 G.-Y. Chen, Z.-Y. Wei, B. Jin, X.-B. Zhong, H. Wang, W.-X. Zhang, J.-C. Liang and Q. Jiang, *Appl. Surf. Sci.*, 2013, **277**, 268–271.
26 J. Yang, M. Wang, Y. Zhu, H. Zhao, R. Wang and J. Chen, *J. Alloys Compd.*, 2011, **509**, 7657–7661.

27 T. Jiang, Y. Wang, K. Wang, Y. Liang, D. Wu, P. Tsiakaras and S. Song, *Appl. Catal., B*, 2016, **189**, 1–11.
28 J. Xi, Y. Xia, Y. Xu, J. Xiao and S. Wang, *Chem. Commun.*, 2015, **51**, 10479–10482.
29 P. Xu, W. Chen, Q. Wang, T. Zhu, M. Wu, J. Qiao, Z. Chen and J. Zhang, *RSC Adv.*, 2015, **5**, 6195–6206.
30 G. Fu, Z. Cui, Y. Chen, Y. Li, Y. Tang and J. B. Goodenough, *Adv. Energy Mater.*, 2017, **7**, 1601172.
31 G. Zhang, W. Lu, F. Cao, Z. Xiao and X. Zheng, *J. Power Sources*, 2016, **302**, 114–125.
32 B. Li, Y. Chen, X. Ge, J. Chai, X. Zhang, T. S. Hor, G. Du, Z. Liu, H. Zhang and Y. Zong, *Nanoscale*, 2016, **8**, 5067–5075.
33 Y. J. Sa, K. Kwon, J. Y. Cheon, F. Kleitz and S. H. Joo, *J. Mater. Chem. A*, 2013, **1**, 9992.
34 J. Sanetuntikul and S. Shanmugam, *Nanoscale*, 2015, **7**, 7644–7650.
35 J. Sanetuntikul, C. Chuaicham, Y.-W. Choi and S. Shanmugam, *J. Mater. Chem. A*, 2015, **3**, 15473–15481.
36 N. Ma, Y. Jia, X. Yang, X. She, L. Zhang, Z. Peng, X. Yao and D. Yang, *J. Mater. Chem. A*, 2016, **4**, 6376–6384.
37 M. Prabu, P. Ramakrishnan, P. Ganesan, A. Manthiram and S. Shanmugam, *Nano Energy*, 2015, **15**, 92–103.
38 X. Liu, M. Park, M. G. Kim, S. Gupta, G. Wu and J. Cho, *Angew. Chem., Int. Ed. Engl.*, 2015, **54**, 9654–9658.
39 J. Wang, H. Wu, D. Gao, S. Miao, G. Wang and X. Bao, *Nano Energy*, 2015, **13**, 387–396.
40 B. Li, Y. Chen, X. Ge, J. Chai, X. Zhang, T. S. Hor, G. Du, Z. Liu, H. Zhang and Y. Zong, *Nanoscale*, 2016, **8**, 5067–5075.
41 M. Prabu, P. Ramakrishnan and S. Shanmugam, *Electrochem. Commun.*, 2014, **41**, 59–63.
42 P. Ganesan, P. Ramakrishnan, M. Prabu and S. Shanmugam, *Electrochim. Acta*, 2015, **183**, 63–69.
43 C. Ma, N. Xu, J. Qiao, S. Jian and J. Zhang, *Int. J. Hydrogen Energy*, 2016, **41**, 9211–9218.